Influence of geomagnetic activity on the O I 630.0 and 557.7 nm dayglow

F. Culot, Chantal Lathuillere, Jean Lilensten

Influence of geomagnetic activity on the O I 630.0 and 557.7 nm dayglow

F. Culot, C. Lathuillère, and J. Lilensten
Laboratoire de Planétologie de Grenoble, Grenoble, France

Received 7 July 2004; revised 24 September 2004; accepted 9 November 2004; published 15 January 2005.

[1] The one-dimensional fluid/kinetic code TRANSCAR is used to simulate the effects of geomagnetic activity on the atomic oxygen (^3P-^1D) red and (^1D-^1S) green thermospheric dayglows at 630.0 and 557.7 nm, associated with the modification of the density structure of the neutral atmosphere. It is found that when magnetic activity increases from quiet to strong, the altitude of the peak of both emissions increases by <10%, the peak intensity of the 557.7 nm thermospheric layer decreases by about 40%, and the peak intensity of the 630.0 nm layer remains almost constant. The prevailing production and quenching processes are reviewed and their variations are explained in terms of changes in the ionospheric and thermospheric parameters which are induced by the rise of the geomagnetic activity. Together with this model study a 4-year set of WINDII data is analyzed. The measurements confirm the trends previously revealed by the TRANSCAR model. No statistical variation of the 630.0 nm peak emission is seen, while the anticorrelation between the 557.7 nm thermospheric peak intensity and the magnetic activity is clearly found.

Citation: Culot, F., C. Lathuillère, and J. Lilensten (2005), Influence of geomagnetic activity on the O I 630.0 and 557.7 nm dayglow, *J. Geophys. Res.*, *110*, A01304, doi:10.1029/2004JA010667.

1. Introduction

[2] The mechanisms responsible for the perturbations appearing in the Earth's high atmosphere during an increase of the geomagnetic activity are well understood today. At high latitudes, energetic particle precipitations increase in the auroral oval, and ionospheric currents intensify, resulting, among other things, in heating by Joule effect. In terms of energy budget this second process is preponderant, the energy supply by Joule heating being at least 2 times greater than the energy supplied during particle precipitation [*Ahn et al.*, 1983; *Knipp et al.*, 2004]. A detailed explanation of the geomagnetic storm effects on the thermosphere can be found in several papers [see, e.g., *Burns et al.*, 1995; *Fuller-Rowell et al.*, 1997], and therefore the major processes that drive changes in the upper atmospheric composition will not be described again here.

[3] However, to summarize the expected changes, one can say that the global disturbances of the thermosphere during magnetically active conditions lead to the heating and expansion of the thermosphere, bringing higher exospheric temperatures and a larger total density. This has been known for 3 decades [*Taeusch et al.*, 1971] and has been statistically described in empirical models [*Jacchia*, 1971; *Barlier et al.*, 1978; *Hedin*, 1983].

[4] These modifications of the neutral atmosphere associated with magnetic activity result in ionospheric changes. At middle latitudes, negative storms prevail in the summer (i.e., decrease in the peak electron density), and positive storms prevail in the winter [*Fuller-Rowell et al.*, 1996]. Development of empirical modeling of storm-time ionospheric response is under way [*Araujo-Pradere et al.*, 2004].

[5] Ionospheric and thermospheric changes, associated with magnetic activity, are expected to induce modifications in the thermospheric dayglow. This is the case for the O I 557.7 nm thermospheric emission: *Zhang and Shepherd* [2000] reported a severe depletion in the thermospheric O(^1S) dayglow during the 4–5 April 1993 storm, when *Kp* reached values of nearly 8. *Wiens et al.* [2002] also reported changes in the 557.7 nm daytime volume emission rate at 250 km during magnetically active conditions, but this work was constrained to low latitudes at equinox.

[6] Our work aims to evaluate if the thermospheric emissions, which represent tracers of the state of the atmosphere, could be used to quantify the influence of geomagnetic activity. It wants to give a global picture of both the red and thermospheric green oxygen emission answer to geomagnetic activity, apart from the effects of precipitations at high latitudes, which will not be investigated here. This study relies on the use of the TRANSCAR model, which allows us to evaluate the emission variations during magnetically active periods. These trends are then compared with a 4-year set of WINDII measurements. Both the modeling and the measurements analysis are limited to low and middle latitudes in order to avoid the particle precipitation influence.

2. TRANSCAR Modeling

2.1. Presentation and Conditions of Use

[7] The TRANSCAR model used in this study is a one-dimensional time-dependent fluid model coupled to a ki-

0148-0227/05/2004JA010667

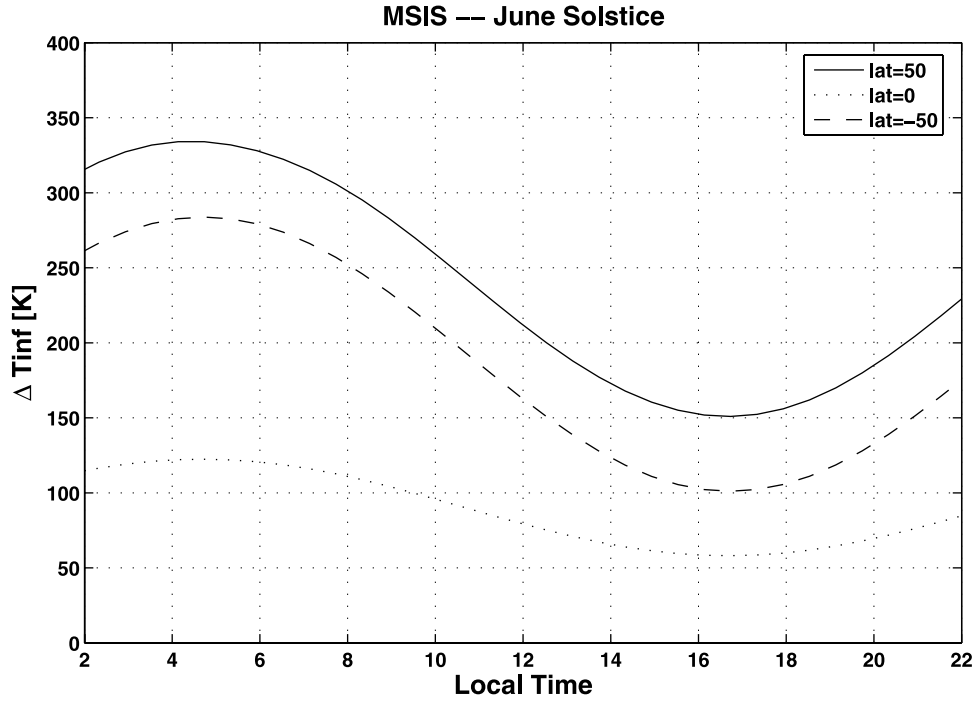

Figure 1. MSIS-90 modeling of the exospheric temperature difference between $Ap = 200$ and $Ap = 10$ on the June solstice day. The different curves represent three different latitudes: 50° (solid line), 0° (dotted line), and −50° (dashed line). These temperature differences are plotted versus local time.

netic suprathermal electron transport model. A complete description of TRANSCAR can be found in work by *Lilensten and Blelly* [2002], including the mathematical formulation, inputs, outputs, and limitations. This model, which describes the ionosphere between 100 and 3000 km altitude, has been extended to calculate the entire profile of the 630.0 and 557.7 nm thermospheric dayglows. It has already shown its ability to describe the high-latitude dayglow [*Witasse et al.*, 1999], and *Culot et al.* [2004] showed that its use can be extended to midlatitudes and low latitudes.

[8] The main inputs of TRANSCAR are the neutral atmosphere, described by the Mass Spectrometer Incoherent Scatter-90 (MSIS-90) empirical model [*Hedin*, 1991], and the EUV solar spectrum, described by the EUVAC model [*Richards et al.*, 1994]. The solar activity index $f_{10.7}$ is used to specify the EUV spectrum. It is also an input to the neutral atmosphere model. In addition, the daily *Ap* index or the 3-hour indices *ap* are used in MSIS-90 for describing the magnetic activity dependence of the neutral constituents and temperature.

[9] For this study it was chosen to run the TRANSCAR model in such conditions that the influence of the magnetic activity would be clearly noticeable. For that purpose the MSIS model was used first to select the period of year and the location that would be favorable to such a study, that is, for which the differences of the atmosphere parameters due to magnetic activity would be as large as possible. We used a solar flux index $f_{10.7}$ equal to 150 (medium solar activity conditions).

[10] Figure 1 shows the difference in exospheric temperature between quiet and very strong magnetic activity. For quiet conditions we run MSIS-90 with a daily *Ap* index equal to 10 and for very disturbed conditions with an *Ap* index of 200 (*Araujo-Pradere et al.* [2004] consider there to be a magnetic storm when $Ap > 150$). The different latitudes 50°, 0°, and −50° are represented by a solid line, a dotted line, and a dashed line, respectively. The temperature perturbation is plotted versus the local time, and this run was performed for the June solstice so that the summer hemisphere is represented by the solid line, while the winter hemisphere is represented by the dashed line. It is noticeable that when approaching the equator, the temperature perturbation diminishes. At greater latitudes the temperature perturbation is more important in the summer hemisphere.

[11] In this study, it was chosen to perform the TRANSCAR model runs at a latitude of 50° during the June solstice, for $f_{10.7} = 150$, and with $Ap = 10$ and $Ap = 200$. Using two different *Ap* values in TRANSCAR induced changes only in the density structure of the atmosphere, while maintaining identical solar EUV ionizing radiation. This procedure will therefore allow us to evaluate the changes in the thermospheric dayglows due to magnetic activity. However, it relies on the ability of the MSIS model to correctly describe the magnetic activity neutral atmosphere perturbations, and it is known that empirical models most often underestimate these perturbations [see, e.g., *Richards*, 2002; *Lathuillère and Menvielle*, 2004]. This will be kept in mind while comparing simulation results and experimental data.

2.2. Results

2.2.1. Atomic Oxygen Red Emission

[12] Figure 2 shows the inputs and the results of TRANSCAR runs related to the red line emission. On the left side of Figure 2, from top to bottom, are shown the

exospheric temperature, the concentration ratios (concentrations at $Ap = 200$ over concentrations at $Ap = 10$) for O and O_2, and the electron density at an altitude of 250 km. These parameters are plotted versus the solar zenith angle (SZA), which is one of the main parameters that influences the intensity of the dayglow [see *Culot et al.*, 2004]. On the right side of Figure 2 are shown the red line peak intensity (taken at the altitude of the maximum) and peak altitude, together with the preponderant production processes at SZA = 50°, the solar zenith angle for which the largest changes are observed with respect to magnetic activity. The solid lines represent parameters calculated with $Ap = 10$, while the dashed lines stand for parameters calculated with $Ap = 200$.

[13] In the top right plot of Figure 2 one can see that the red line peak intensity remains almost identical when changing from a weak to a strong magnetic activity. The largest difference is noticeable around SZA = 50°, with an emission intensity greater by about 5% when $Ap = 200$. Concerning the maximum emission altitude (middle right plot of Figure 2), when magnetic activity increases, the emission gets higher by about 10%, whatever the SZA. A closer look at the variations in production and loss processes is needed to understand these trends. Regarding the production processes, the bottom right plot of Figure 2 shows the three main reactions responsible for the red line: the dissociative recombination (in green) ($O_2^+ + e_{th} \rightarrow O + O(^1D)$), the photoelectron impacts on atomic oxygen (in blue) ($O + e_{ph} \rightarrow O(^1D) + e_{ph}$), and photodissociation of molecular oxygen (in cyan) ($O_2 + h\nu \rightarrow O + O(^1D)$).

[14] Around the emission peak maximum the reaction involving the photoelectron impacts has a volume emission rate that remains almost constant but with a contribution shifted by about 40 km upward. The dissociative recombination decreases below 270 km but increases above, and the photodissociation increases whatever the altitude considered. The large increase in photodissociation of molecular oxygen is due to the rise in O_2 concentration, which is multiplied by almost 4 at 250 km, as seen in the middle left plot of Figure 2. On the other hand, the decrease in dissociative recombination below 270 km is due to the strong diminution of the electron concentration at these altitudes (corresponding to negative storm conditions), as shown in the bottom left plot of Figure 2 with a loss of more than 60% for SZA smaller than 70°.

[15] At the peak altitude and below, quenching of the O^1D excited state with molecular nitrogen is the prevailing deactivation process. The rise in N_2 concentration (see the middle left plot in Figure 2) will therefore induce an increase in losses. This loss increase and the opposite variations of the main production processes result in an almost constant red line peak emission intensity, even though the maximum emission altitude increases slightly (by about 10%) mainly because of the upward shift of the dissociative recombination and the reaction involving the photoelectron impacts.

2.2.2. Atomic Oxygen Green Thermospheric Emission

[16] Figure 3 shows the results of TRANSCAR runs related to the green line thermospheric emission. The bottom plots indicate the green line volume emission rates (taken at the altitude of the maximum), together with the preponderant production processes, for SZA = 30° (left) and SZA = 70° (right). These production processes are as follows: collisional deactivation of N_2 (in cyan) ($N_2(A^3\Sigma_u^+) + O \rightarrow N_2 + O(^1S)$), the photoelectron impacts on atomic oxygen (in blue) ($O + e_{ph} \rightarrow O(^1S) + e_{ph}$), and the dissociative recombination (in green) ($O_2^+ + e_{th} \rightarrow O + O(^1S)$).

[17] The plots on the left side of Figure 3 show the concentration ratios of the main concerned species ([O], $[N_2]$, $[N_2]^*$, and N_e), in the same way as for the red emission, but for an altitude of 150 km. Also shown are the photoelectron profiles at an energy of 6 eV, which is the energy needed to get the excitation of the N_2 Vegard-Kaplan band involved in the reaction of collisional deactivation [*Meier*, 1991]. The plots on the right side of Figure 3 indicate the intensity and altitude of the green line thermospheric peak.

[18] As for the O I 630.0 nm emission, the peak altitude gets higher with the increase of the geomagnetic activity, and this rise is also about 10%. Concerning the intensity of the thermospheric peak, a strong decrease is noticeable, which represents a loss of about 40% at all the different SZAs.

[19] When looking at the production processes, one can see that the collisional deactivation of N_2 is the major production process. Its decrease in intensity can be understood when looking at the variation in $N_2(A^3\Sigma_u^+)$ in the top left plot of Figure 3: While the N_2 concentration rises by a factor of 1.5, the concentration in N_2 excited state declines significantly with the SZA. This excited state is produced by photoelectron impacts, and it is shown in the middle left plot of Figure 3 that their concentration becomes less important when Ap increases, and then the impacts on N_2 molecules become more sporadic.

[20] The second important reaction, which involves the photoelectron impacts, also becomes weaker at low altitudes with the rise of the magnetic activity, and this is once again due to the decrease in photoelectron concentration below 200 km. When looking at higher altitudes, the contribution of these two prevailing reactions increases because of the rise in photoelectron flux above 200–240 km, depending on the considered SZA (see the middle left plot of Figure 3). This photoelectron flux acts directly on the reaction involving impacts on atomic oxygen and, as explained above, is also responsible for the $N_2(A^3\Sigma_u^+)$ concentration.

[21] The last reaction, namely, the dissociative recombination, sees its contribution diminishing because of the decrease in electronic density, as shown in the top left plot of Figure 3. Regarding the loss processes, since the radiative lifetime of the $O(^1)$ state is only about 1 s, the collisional deactivation can be neglected compared with emission.

[22] We have seen now that the three major production reactions involved in the production of the 557.7 nm thermospheric peak become weaker below about 200 km and rise above when the geomagnetic activity increases. As a result, the thermospheric peak intensity decreases also when the geomagnetic activity becomes stronger, and the emission altitude shifts upward by about 10%.

3. WINDII Measurements

3.1. Instrument

[23] The dayglow measurements are derived from the WIND Imaging Interferometer (WINDII), which was

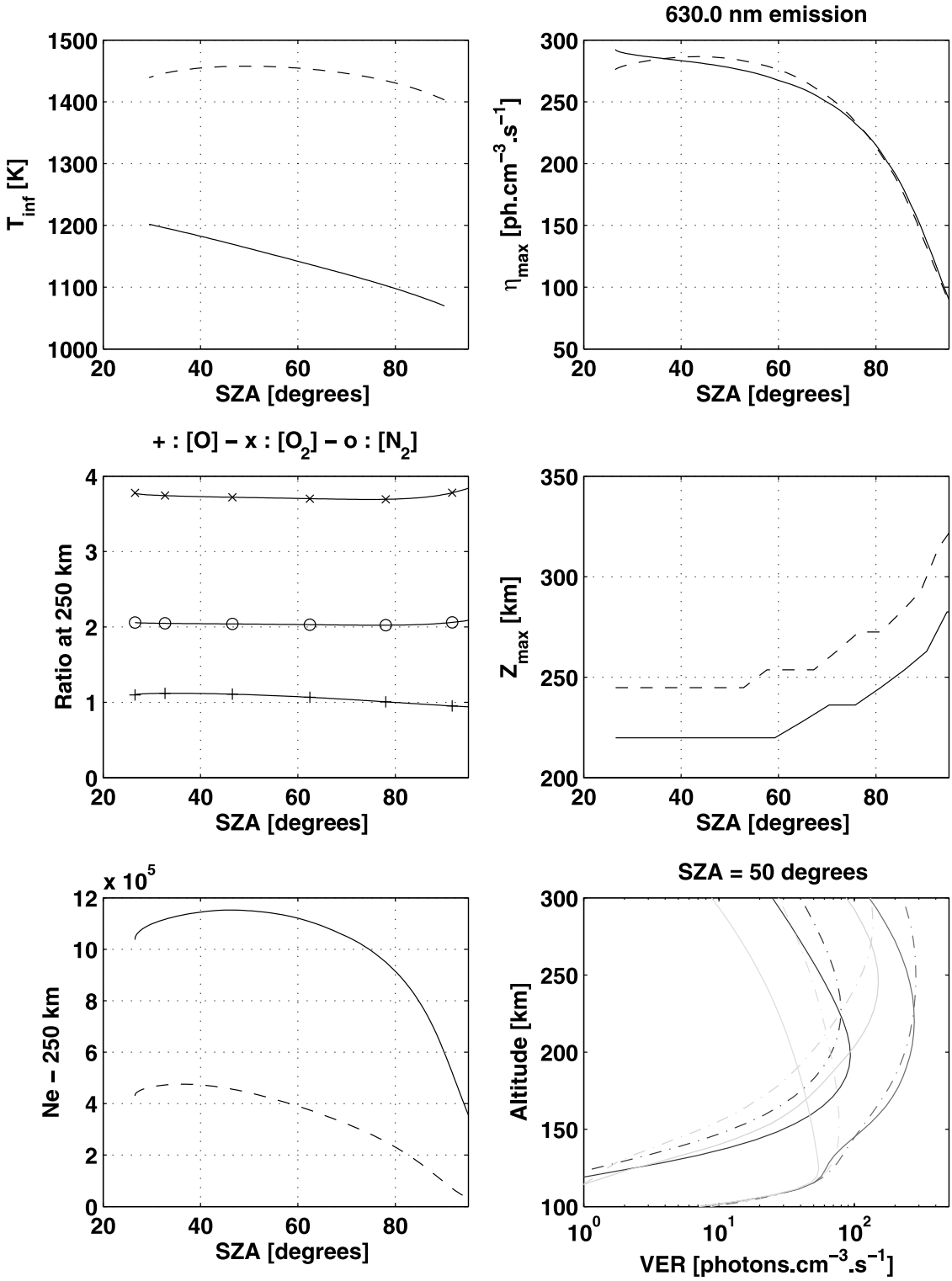

Figure 2. TRANSCAR modeling of the atomic oxygen red line emission and related parameters for quiet magnetic activity (solid lines) and strong magnetic activity (dashed lines). The top and middle plots on the right show the emission at the peak of the layer and the peak altitude as a function of solar zenith angle (SZA). The bottom right plot shows the three main reactions responsible for the 630.0 nm emission (in red) for an SZA of 50°: the dissociative recombination (green), the photoelectron impacts on atomic oxygen (blue), and the photodissociation of molecular oxygen (cyan). The three plots on the left show (from top to bottom) the exospheric temperature, the ratio of the neutral densities for strong magnetic activity to their values for quiet magnetic activity at 250 km altitude, and the electron densities at 250 km altitude. See color version of this figure at back of this issue.

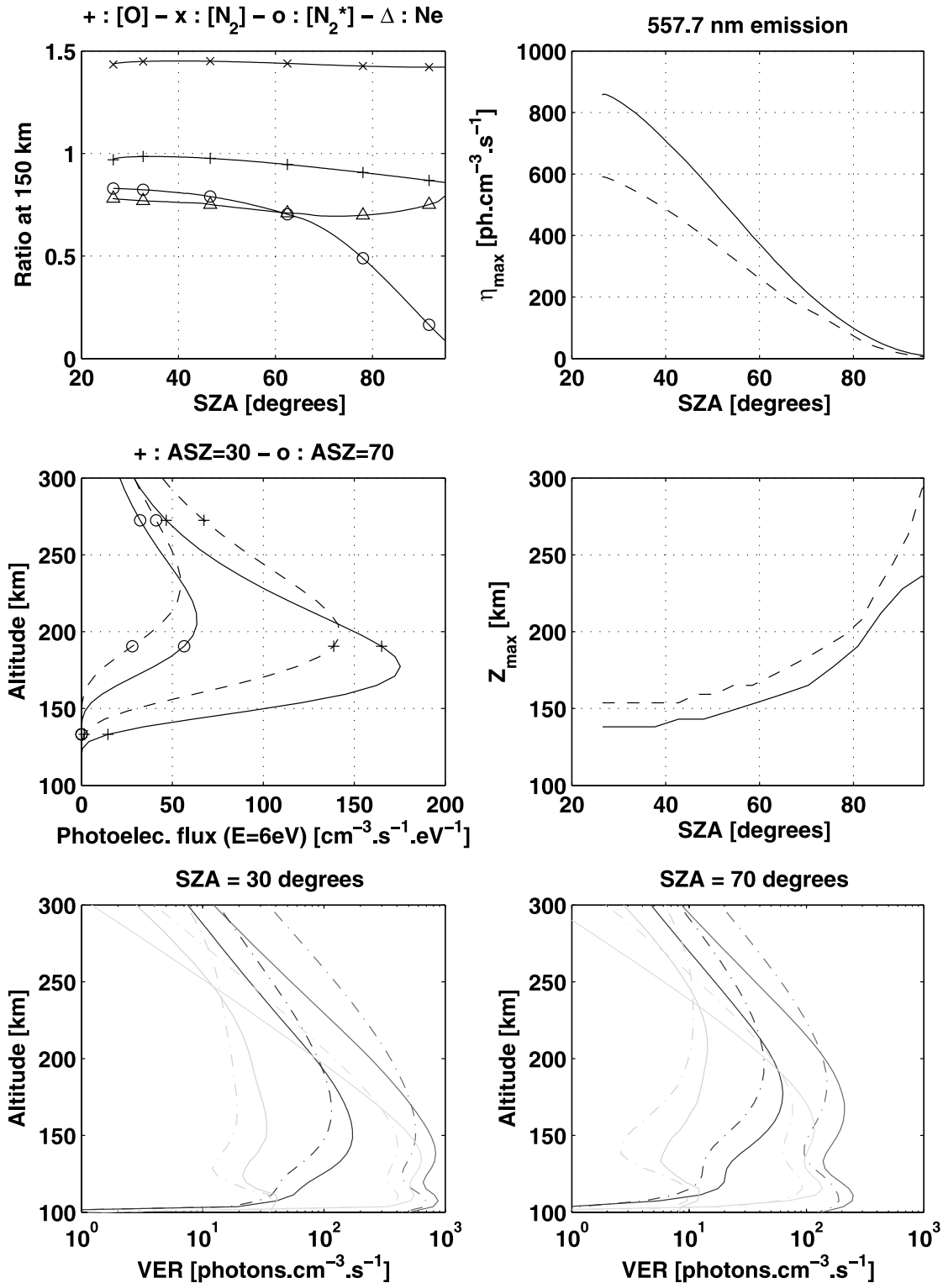

Figure 3. TRANSCAR modeling of the atomic oxygen green line emission and related parameters for quiet magnetic activity (solid lines) and strong magnetic activity (dashed lines). The top and middle panels on the right show the emission at the peak of the layer and the peak altitude as a function of solar zenith angle (SZA). The bottom plots show the three main reactions responsible for the 557.7 nm emission (in red) for (left) an SZA of 30° and (right) an SZA of 70°: the collisional deactivation of N_2 (cyan), the photoelectron impacts on atomic oxygen (blue), and the dissociative recombination (green). The top left plot shows the ratio of O, N_2, and N_2 excited state and electron densities for strong magnetic activity to their values for quiet magnetic activity at 150 km altitude. The middle left plot shows the photoelectron flux at an energy of 6 eV for SZA = 30° and SZA = 70°. See color version of this figure at back of this issue.

launched on 12 September 1991 on NASA's UARS, a satellite dedicated to upper atmosphere studies [*Reber et al.*, 1993]. The most detailed description of the instrument can be found in work by *Shepherd et al.* [1993]. WINDII allows us to obtain the volume emission rates of the $O(^1S)$, $O(^1D)$, OH, and O_2 lines, corresponding to an altitude ranging from 80 to 300 km. Error bars on the volume emission rates are about 1–10 photons cm^{-3} s^{-1}.

3.2. Volume Emission Rates Obtained Using Zonal Average

[24] In a previous paper [*Culot et al.*, 2004], statistical results obtained using zonally averaged WINDII data showed the evolution of the oxygen emissions with the solar flux. This previous study concerns quiet magnetic days ($Ap \leq 10$). The same study is performed here but for stronger magnetic activity.

3.2.1. Atomic Oxygen Red Emission

[25] Figure 4 shows the intensity and altitude of the 630.0 nm red line peak versus the Mg II proxy [*Heath and Schlesinger*, 1986], which has been shown to better characterize the solar activity effect on O^1D as compared with $f_{10.7}$ [*Culot et al.*, 2004]. The Mg II range (0.26–0.28) used in Figure 4 corresponds to an $f_{10.7}$ range going from 70 to about 200. The black dots correspond to quiet magnetic days, and this data set is identical to the one previously published by *Culot et al.* [2004], while the green data set corresponds to days for which $Ap > 10$.

[26] The two separated categories of magnetic activity do not show clear discrepancies while looking at the intensity and altitude of maximum emission, while we had a 10% increase in altitude with TRANSCAR modeling. This is not incompatible with the model results as long as the WINDII data set for the red line is not large enough to draw clear conclusions. However, this trend showing an almost constant emission rate intensity is similar to the one found by TRANSCAR for negative storm conditions (see section 2.2.1).

3.2.2. Atomic Oxygen Green Thermospheric Emission

[27] No differences could be found on the oxygen red emission, but on the other hand, variations can be found when looking at Figure 5, which represents thermospheric green line data. Again, the black dots correspond to the data set previously published for which the magnetic activity was quiet ($Ap \leq 10$), and the green data set stands for more magnetically active conditions ($Ap > 30$), that is, about 30 days with 5 days around $Ap \approx 200$.

[28] At SZA = 30° (top plots in Figure 5) the small number of available days is not sufficient to draw any conclusion, and at 70° (bottom plots in Figure 5) the differences between the two data sets are not visible, which was expected when looking at the TRANSCAR results in the top right plot of Figure 3. However, for 50° (middle plots in Figure 5), it is noticeable that the peak emission intensity becomes weaker and the maximum emission altitude increases when magnetic activity rises.

[29] We find again here the trends we had been able to exhibit in section 2.2 using the TRANSCAR model, which makes us believe that the variations induced by the rise in magnetic activity were properly taken into account. To make a quantitative comparison with TRANSCAR results, a more precise study using green line data from each orbit, and without any zonal averaging, was performed.

3.3. Green Line Trends

[30] A great variability is noticeable in the intensity and altitude of the emissions when looking at the different WINDII orbits, and using a zonal averaging smooths this variability. Thus, to obtain a better quantification of the influence of the magnetic activity on the intensity and altitude of the green line thermospheric peak, data around 50° in latitude from each orbit were taken into account and were analyzed as explained in this section. Three steps are involved in this analysis: (1) subtraction of the solar flux and SZA influence, (2) linking of each orbit and the magnetic activity index, and (3) computation of the confidence intervals.

[31] First, it was necessary to subtract the solar flux and SZA influence. To do so, a linear regression was performed on the green line data using the quiet magnetic days obtained by *Culot et al.* [2004] and presented in Figure 5 as the red line. The obtained linear fits are as follows: for SZA = 30°, $\langle \eta_{max} \rangle = 17{,}915 \times \text{Mg II} - 4102$ and $\langle Z_{max} \rangle = 369 \times \text{Mg II} - 43.8$; for SZA = 50°, $\langle \eta_{max} \rangle = 12610 \times \text{Mg II} - 2911$ and $\langle Z_{max} \rangle = 687.2 \times \text{Mg II} - 34.8$; and for SZA = 70°, $\langle \eta_{max} \rangle = 6077 \times \text{Mg II} - 1419$ and $\langle Z_{max} \rangle = 826.1 \times \text{Mg II} - 54.7$. This regression was then subtracted from the measurements done during geomagnetically active days so that only the variations due to this magnetic activity remain.

[32] The second step consisted of getting the magnetic index *Kp* corresponding to the 3 hours preceding the considered orbit. The *Kp* index follows a logarithmic scale, and the conversion from *Kp* to *Ap* can be found in work by *Menvielle and Berthelier* [1991]. To give an example, a *Kp* of 2 is equal to an *Ap* of about 7, and a *Kp* of 8 is equal to an *Ap* of about 200.

[33] The 3-hour magnetic index is a key input to specify the geomagnetic activity, as exposed by *Hedin* [1983]. Moreover, *Hecht et al.* [1991] showed that the MSIS model gives better results when used with a 3-hour magnetic index because during storm periods, large changes occur over short time periods, and these changes are best transcribed with this proxy. Last, considering the previous 3-hour period allows us to take into account the delay in the thermospheric density and temperature response after a heating event, as was chosen by *Holt et al.* [2002] in their ionospheric model, as well as *Lathuillère and Menvielle* [2004] in their study on characterizing geomagnetic activity in subauroral regions. This time lag is also estimated by *Berger et al.* [1998] to be between 3 hours at the poles and 6 hours at the equator, and thus the 3-hour delay corresponds to the latitudes around 50° considered in this study.

[34] The last step in this analysis consisted of computing the expected values with a 95% confidence interval, assuming that the actual data statistical distribution can be considered as a Student one. Large confidence intervals correspond to situations for which few observations were available.

[35] Figure 6 shows the obtained results for the intensity of the thermospheric peak. One can notice a decrease in the peak intensity with the increase in magnetic activity. This decrease is roughly 40% when going from very weak

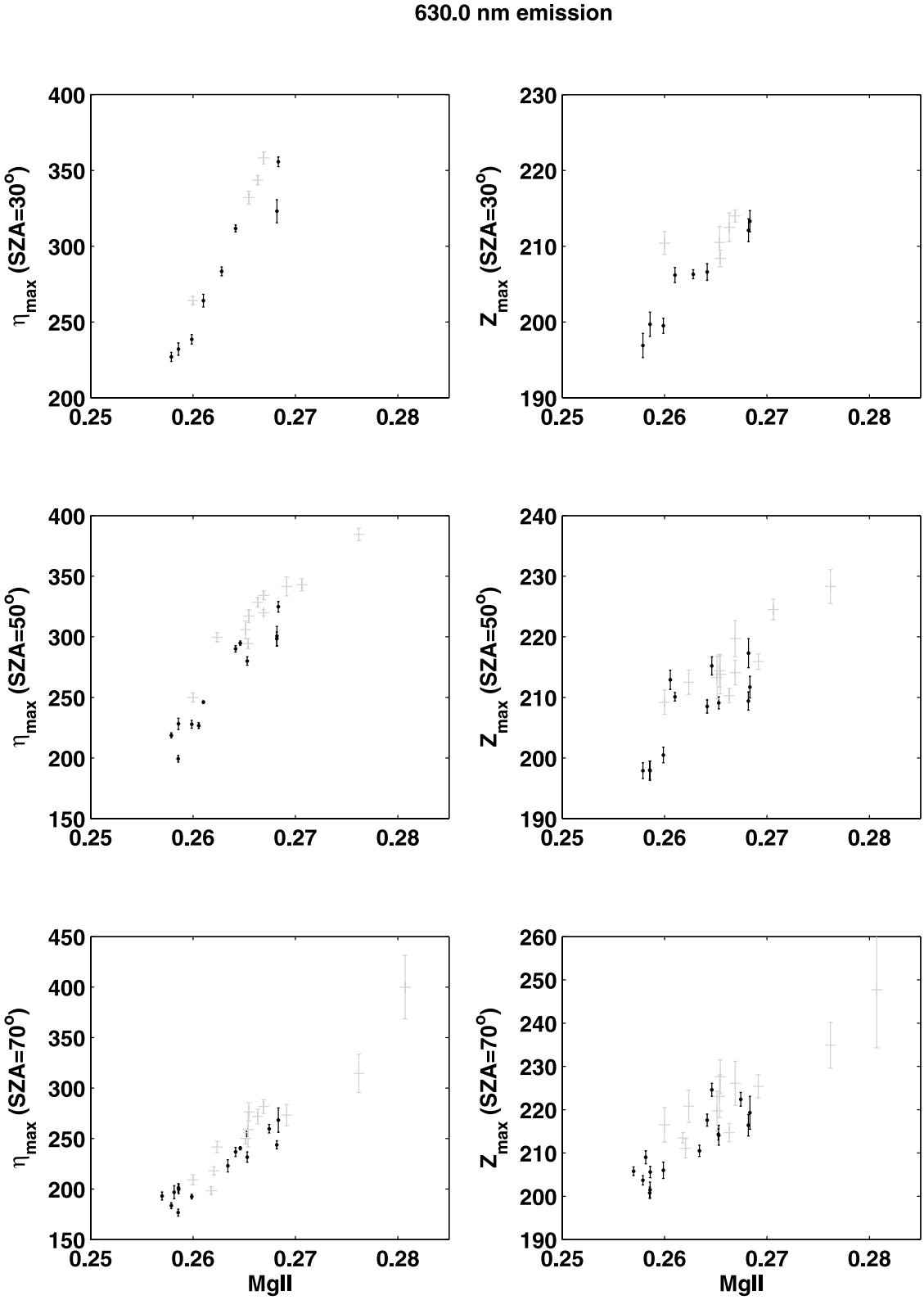

Figure 4. WINDII measurements of the 630.0 nm volume emission rates (taken at the altitude of the maximum) and peak altitudes from 1992 to 1995. The volume emission rate (η) is expressed in photons cm^{-3} s^{-1}, and the altitude Z_{max} is expressed in km. Data are plotted versus the Mg II proxy, and error bars correspond to the standard deviation. The black data set corresponds to quiet geomagnetic days ($Ap \leq 10$), while the green data set corresponds to stronger geomagnetic activity ($Ap > 10$). See color version of this figure at back of this issue.

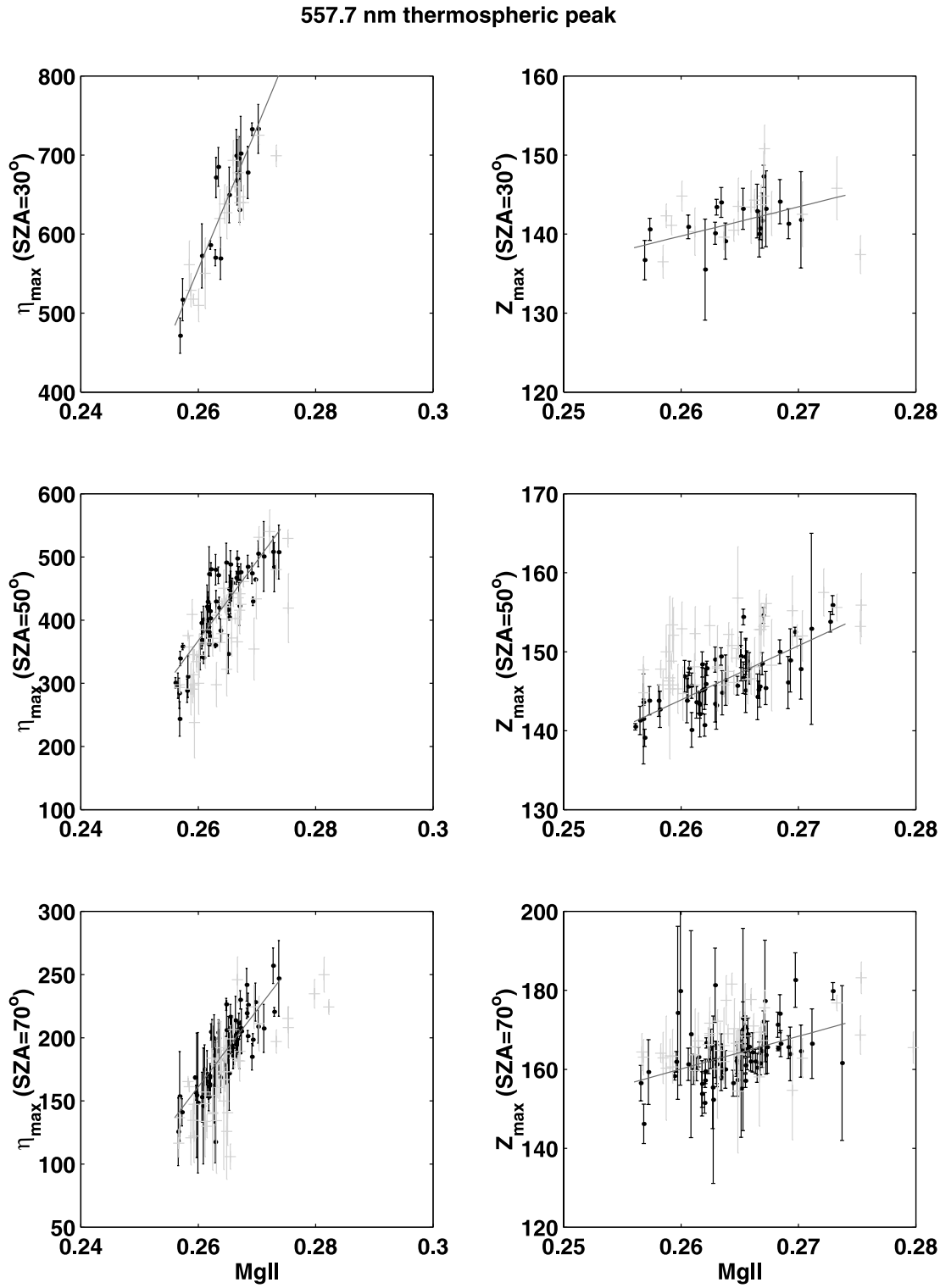

Figure 5. WINDII measurements of the thermospheric peak of the 557.7 nm emission from 1992 to 1995. The volume emission rate (η) is expressed in photons cm^{-3} s^{-1}, and the altitude Z_{max} is expressed in km. Data are plotted versus the Mg II proxy, and error bars correspond to the standard deviation. The black data set corresponds to quiet geomagnetic days ($Ap \leq 10$), the red line being the related linear regression, while the green data set corresponds to stronger geomagnetic activity ($Ap > 30$). See color version of this figure at back of this issue.

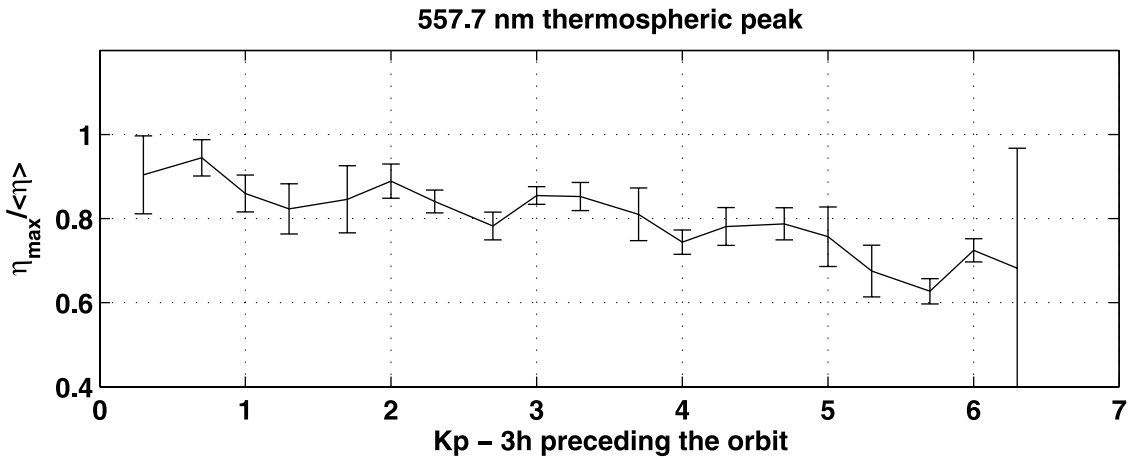

Figure 6. Intensity of the thermospheric peak (taken at the altitude of the maximum) of the oxygen 557.7 nm emission, plotted versus the 3-hour *Kp* index preceding the measurements. The vertical bars correspond to the 95% confidence intervals.

activity to $Kp > 6$. The same work was done on the emission altitude, showing a small increase which did not exceed 10% and thus was not plotted here.

[36] TRANSCAR results exposed in section 2.2.2, and corresponding to 50° in latitude, show a green line thermospheric intensity decreasing by about 40% with the increase in geomagnetic activity to an *Ap* of 200, whatever the SZA considered. This 40% decrease in the observed emissions is found for $Kp = 6$. This *Kp* of 6 is equivalent to an *Ap* of about 90, which is smaller than the $Ap = 200$ for which TRANSCAR was run. This is not surprising because for strong magnetic conditions, neutral atmosphere models are known to underestimate temperature [*Lathuillère and Menvielle*, 2004] and density perturbations [*Burns et al.*, 1991]. The fact that TRANSCAR is able to reproduce these trends observed during magnetic storms indicates that this model represents a useful tool to study the high-atmosphere response to geomagnetic activity, which is important for space weather users.

4. Summary and Conclusion

[37] In summarizing the behavior of the atomic oxygen emissions with regard to the geomagnetic activity, there are two estimations of this parameter's influence:

[38] 1. The influence of geomagnetic activity is noticeable on the altitude and intensity of the oxygen green line thermospheric peak, while it has very little effect on the oxygen red line.

[39] 2. When the magnetic index *Kp* increases from 0 to >6, the intensity of the green line thermospheric peak decreases by about 40%, and the emission altitude increases by <10%. This behavior is mainly caused by the diminution of the production process involving the collisional deactivation of $N_2(A^3\Sigma_u^+)$.

[40] This behavior related to the geomagnetic activity is appropriately estimated by our one-dimensional fluid/kinetic model TRANSCAR. This work takes place in the frame of space weather research. One issue of space weather is to monitor the thermosphere in order to ameliorate satellite drag models and forecasts. A possible way to do so is to use the emission lines of the thermosphere, especially the two of interest in this study, namely, the red and green ones, since they are among the most intense. From this study it turns out that the intensity of the green line thermospheric peak could be a good candidate as a thermosphere proxy, but the red line can hardly be used for this purpose. In the near future we will explore how the information given by the green line can be used along with the total electron content values from global positioning systems in order to monitor the coupled ionosphere-thermosphere system.

[41] **Acknowledgments.** Arthur Richmond thanks Dirk Lummerzheim and Jonathan Makela for their assistance in evaluating this paper.

References

Ahn, B.-H., S. I. Akasofu, and Y. Kamide (1983), The Joule heat production rate and the particle energetic injection rate as a function of the geomagnetic indices *AE* and *AL*, *J. Geophys. Res.*, *88*, 6275.

Araujo-Pradere, E. A., T. J. Fuller-Rowell, M. V. Codrescu, and A. Anghel (2004), Evaluation and prospects for storm-time corrections in the International Reference Ionosphere, *Adv. Space Res.*, *33*, 902.

Barlier, F., C. Berger, J. L. Falin, G. Kockarts, and G. Thuillier (1978), A thermospheric model based on satellite drag data, *Ann. Geophys.*, *34*, 9.

Berger, C., R. Biancale, M. Yii, and F. Barlier (1998), Improvement of the empirical thermospheric model DTM: DTM94—A comparative review of various temporal variations and prospects in space geodesy applications, *J. Geod.*, *72*, 161.

Burns, A. G., T. L. Killeen, and R. G. Roble (1991), A theoretical study of thermospheric composition perturbations during an impulsive geomagnetic storm, *J. Geophys. Res.*, *96*, 14,154.

Burns, A. G., T. L. Killeen, W. Deng, G. R. Carignan, and R. G. Roble (1995), Geomagnetic storm effects in the low- to middle-latitude upper thermosphere, *J. Geophys. Res.*, *100*, 14,673.

Culot, F., C. Latuillère, J. Lilensten, and O. Witasse (2004), The O I 630.0 and 557.7 nm dayglow measured by WINDII and modeled by TRANSCAR, *Ann. Geophys.*, *22*, 1.

Fuller-Rowell, T. J., M. V. Codrescu, H. Rishbeth, R. J. Moffett, and S. Quegan (1996) On the seasonal response of the thermosphere and ionosphere to geomagnetic storms, *J. Geophys. Res.*, *101*, 2343.

Fuller-Rowell, T. J., M. V. Codrescu, R. G. Roble, and A. D. Richmond (1997), How does the thermosphere and ionosphere react to a geomagnetic storm?, in *Magnetic Storms*, *Geophys. Monogr. Ser.*, vol. 98, p. 203, AGU, Washington, D. C.

Heath, D. F., and B. M. Schlesinger (1986), The Mg 280 nm doublet as a monitor of changes in solar ultraviolet irradiance, *J. Geophys. Res.*, *91*, 8672.

Hecht, J. H., D. J. Strickland, A. B. Christensen, D. C. Kayser, and R. L. Walterscheid (1991), Lower thermospheric composition changes derived

from optical and radar data taken at Sondre Stromfjord during the great magnetic storm of February, 1986, *J. Geophys. Res.*, *96*, 5757.
Hedin, A. E. (1983), A revised thermospheric model based on mass spectrometer and incoherent scatter data: MSIS-83, *J. Geophys. Res.*, *88*, 10,170.
Hedin, A. E. (1991), Extension of the MSIS thermosphere model into the middle and lower atmosphere, *J. Geophys. Res.*, *96*, 1159.
Holt, J. M., S.-R. Zhang, and M. J. Buonsanto (2002), Regional and local ionospheric models based on Millstone Hill incoherent scatter radar data, *Geophys. Res. Lett.*, *29*(8), 1207, doi:10.1029/2002GL014678.
Jacchia, L. G. (1971), Revised static models of the thermosphere and exosphere with empirical temperature profiles, *Smithson. Astrophys. Obs.*, *333*, 10,091.
Knipp, D. J., T. Welliver, M. G. McHarg, F. K. Chun, W. K. Tobiska, and D. Evans (2004), Climatology of extreme upper atmospheric events, *Adv. Space Res.*, in press.
Lathuillère, C., and M. Menvielle (2004), WINDII thermosphere temperature perturbation for magneticallay active situations, *J. Geophys. Res.*, *109*, A11304, doi:10.1029/2004JA010526.
Lilensten, J., and P.-L. Blelly (2002), The TEC and F2 parameters as tracers of the ionosphere and thermosphere, *J. Atmos. Sol. Terr. Phys.*, *64*, 775.
Meier, R. R. (1991), Ultraviolet spectroscopy and remote sensing of the upper atmosphere, *Space Sci. Rev.*, *58*, 1.
Menvielle, M., and A. Berthelier (1991), The *K*-derived planetary indices: Description and availability, *Rev. Geophys.*, *29*, 415.
Reber, C. A., C. E. Trevathan, R. J. McNeal, and M. R. Luther (1993), The Upper Atmospheric Research Satellite (UARS) mission, *J. Geophys. Res.*, *98*, 10,643.
Richards, P. G. (2002), Ion and neutral density variations during ionospheric storms in September 1974: Comparison of measurement and models, *J. Geophys. Res.*, *107*(A11), 1361, doi:10.1029/2002JA009278.
Richards, P. G., J. A. Fennelly, and D. G. Torr (1994), EUVAC: A solar EUV flux model for aeronomic calculations, *J. Geophys. Res.*, *99*, 8981.
Shepherd, G. G., et al. (1993), WINDII, the Wind Imaging Interferometer on the Upper Atmosphere Research Satellite, *J. Geophys. Res.*, *98*, 10,725.
Taeusch, D. R., G. R. Carignan, and C. A. Reber (1971), Neutral composition variation above 400 km during a magnetic storm, *J. Geophys. Res.*, *76*, 8318.
Wiens, R. H., V. P. Bhatnagar, and G. Thuillier (2002), Geomagnetic storm heating effects on the low-latitude dayside thermosphere from WINDII observations at equinox, *J. Atmos. Sol. Terr. Phys.*, *64*, 1393.
Witasse, O., J. Lilensten, C. Lathuillère, and P.-L. Blelly (1999), Modelling the O I 630.0 and 557.7 nm thermospheric dayglow during EISCAT-WINDII coordinated measurements, *J. Geophys. Res.*, *104*, 24,639.
Zhang, S. P., and G. G. Shepherd (2000), Neutral winds in the lower thermosphere observed by WINDII during the April 4–5th, 1993 storm, *Geophys. Res. Lett.*, *27*, 1855.

F. Culot, C. Lathuillère, and J. Lilensten, Laboratoire de Planétologie de Grenoble, Bâtiment D de physique, B.P. 53, F-38041 Grenoble cedex 9, France. (frederic.culot@obs.ujf-grenoble.fr)

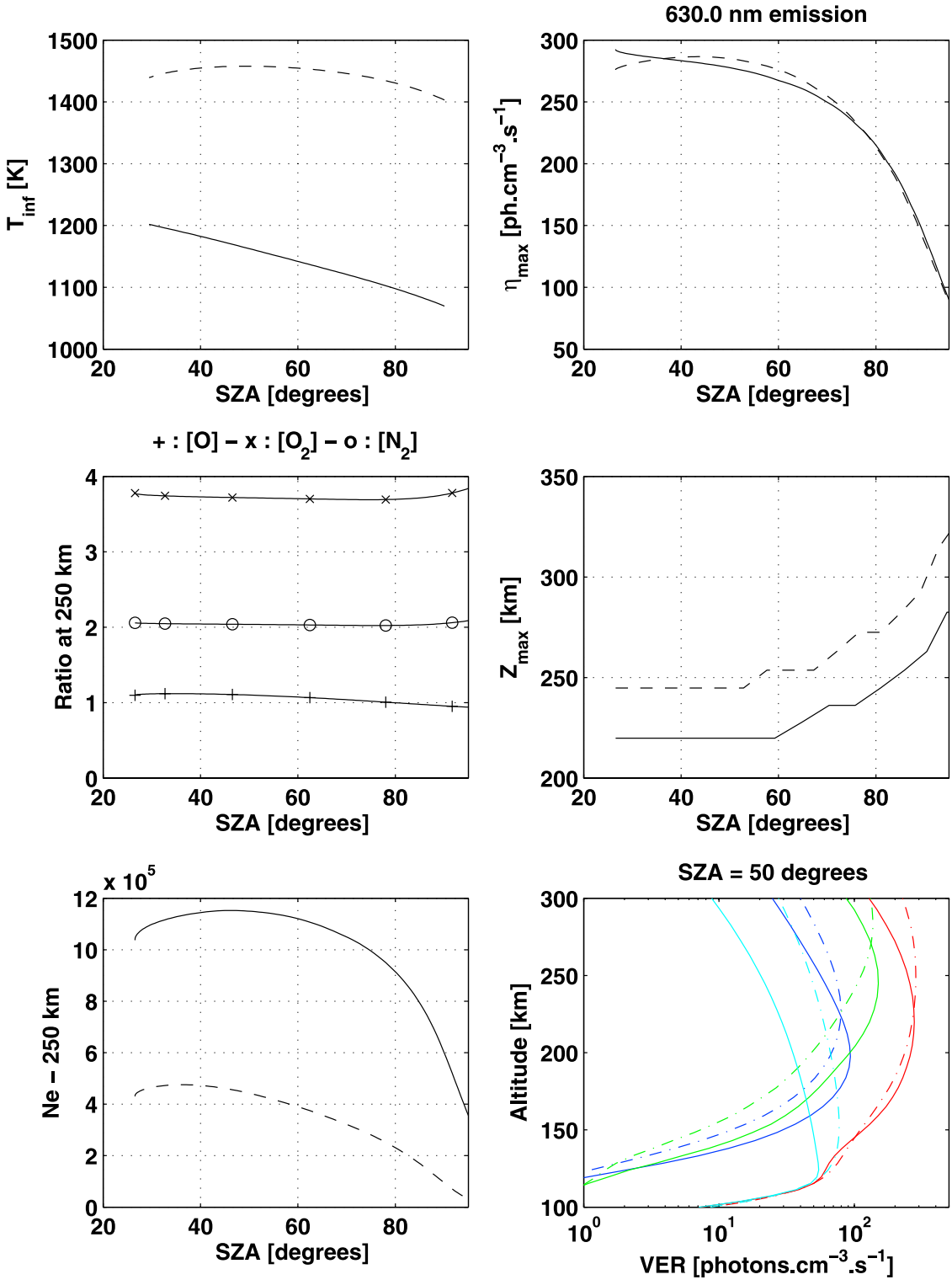

Figure 2. TRANSCAR modeling of the atomic oxygen red line emission and related parameters for quiet magnetic activity (solid lines) and strong magnetic activity (dashed lines). The top and middle plots on the right show the emission at the peak of the layer and the peak altitude as a function of solar zenith angle (SZA). The bottom right plot shows the three main reactions responsible for the 630.0 nm emission (in red) for an SZA of 50°: the dissociative recombination (green), the photoelectron impacts on atomic oxygen (blue), and the photodissociation of molecular oxygen (cyan). The three plots on the left show (from top to bottom) the exospheric temperature, the ratio of the neutral densities for strong magnetic activity to their values for quiet magnetic activity at 250 km altitude, and the electron densities at 250 km altitude.

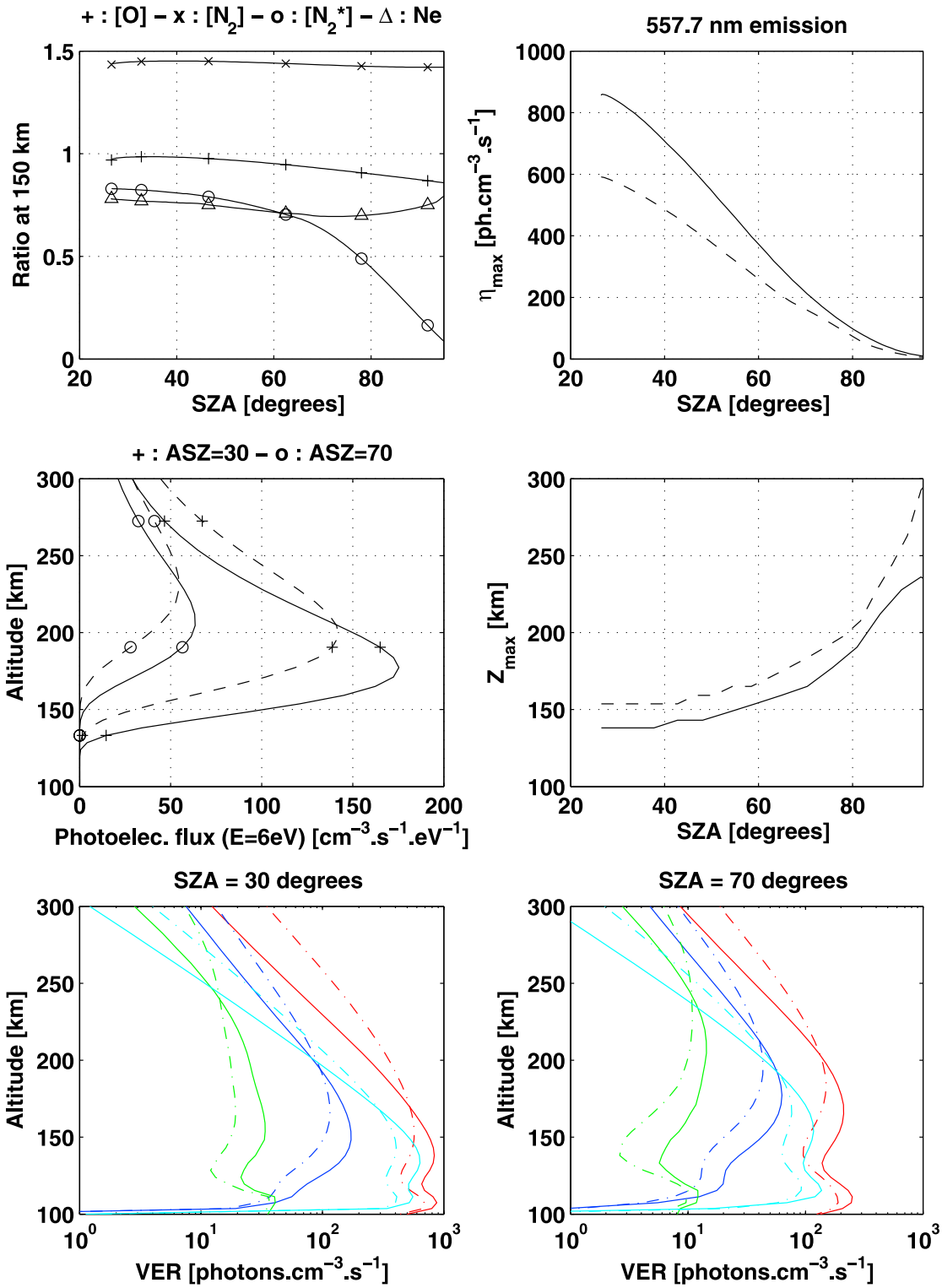

Figure 3. TRANSCAR modeling of the atomic oxygen green line emission and related parameters for quiet magnetic activity (solid lines) and strong magnetic activity (dashed lines). The top and middle panels on the right show the emission at the peak of the layer and the peak altitude as a function of solar zenith angle (SZA). The bottom plots show the three main reactions responsible for the 557.7 nm emission (in red) for (left) an SZA of 30° and (right) an SZA of 70°: the collisional deactivation of N_2 (cyan), the photoelectron impacts on atomic oxygen (blue), and the dissociative recombination (green). The top left plot shows the ratio of O, N_2, and N_2 excited state and electron densities for strong magnetic activity to their values for quiet magnetic activity at 150 km altitude. The middle left plot shows the photoelectron flux at an energy of 6 eV for SZA = 30° and SZA = 70°.

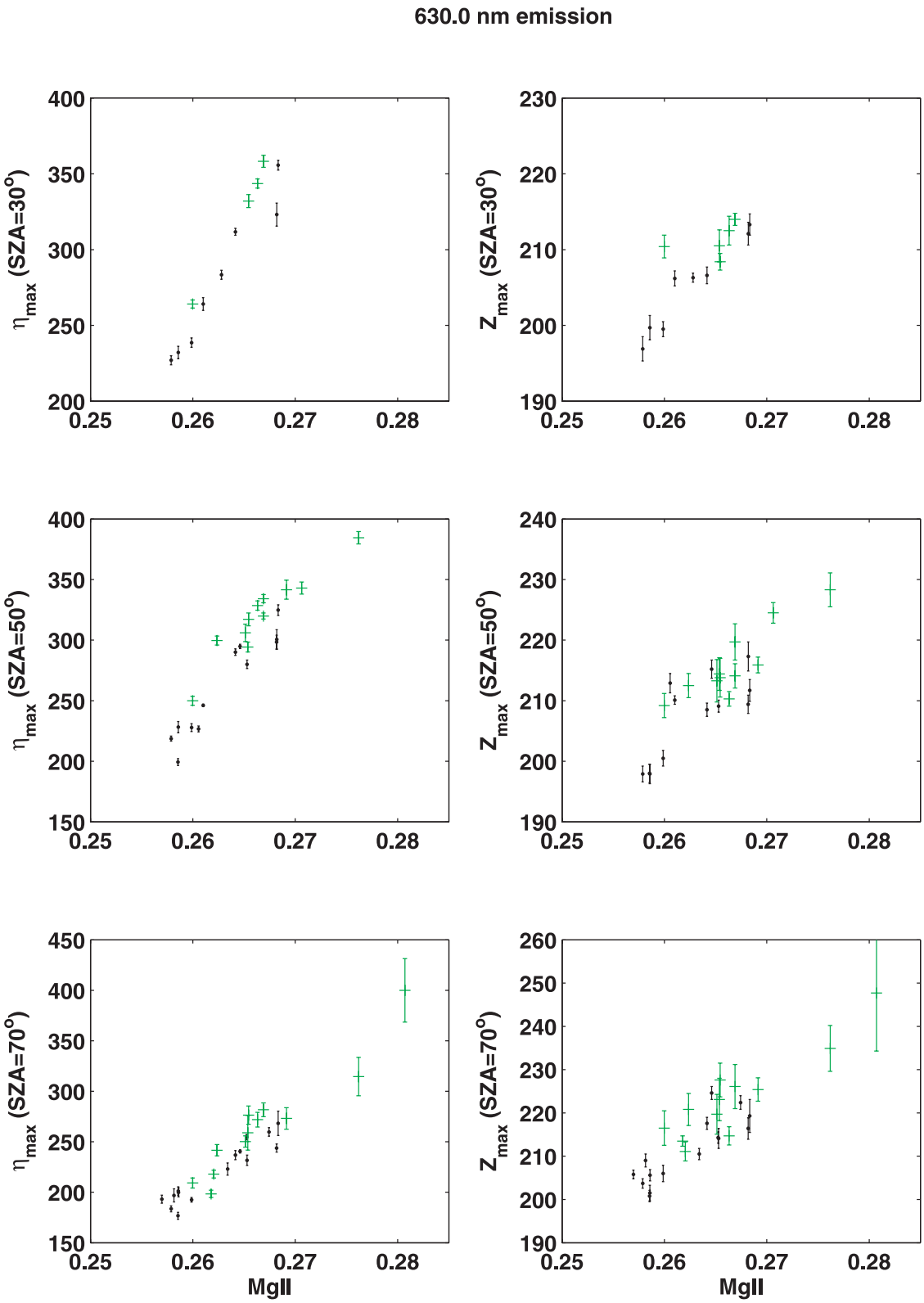

Figure 4. WINDII measurements of the 630.0 nm volume emission rates (taken at the altitude of the maximum) and peak altitudes from 1992 to 1995. The volume emission rate (η) is expressed in photons cm^{-3} s^{-1}, and the altitude Z_{max} is expressed in km. Data are plotted versus the Mg II proxy, and error bars correspond to the standard deviation. The black data set corresponds to quiet geomagnetic days ($Ap \leq 10$), while the green data set corresponds to stronger geomagnetic activity ($Ap > 10$).

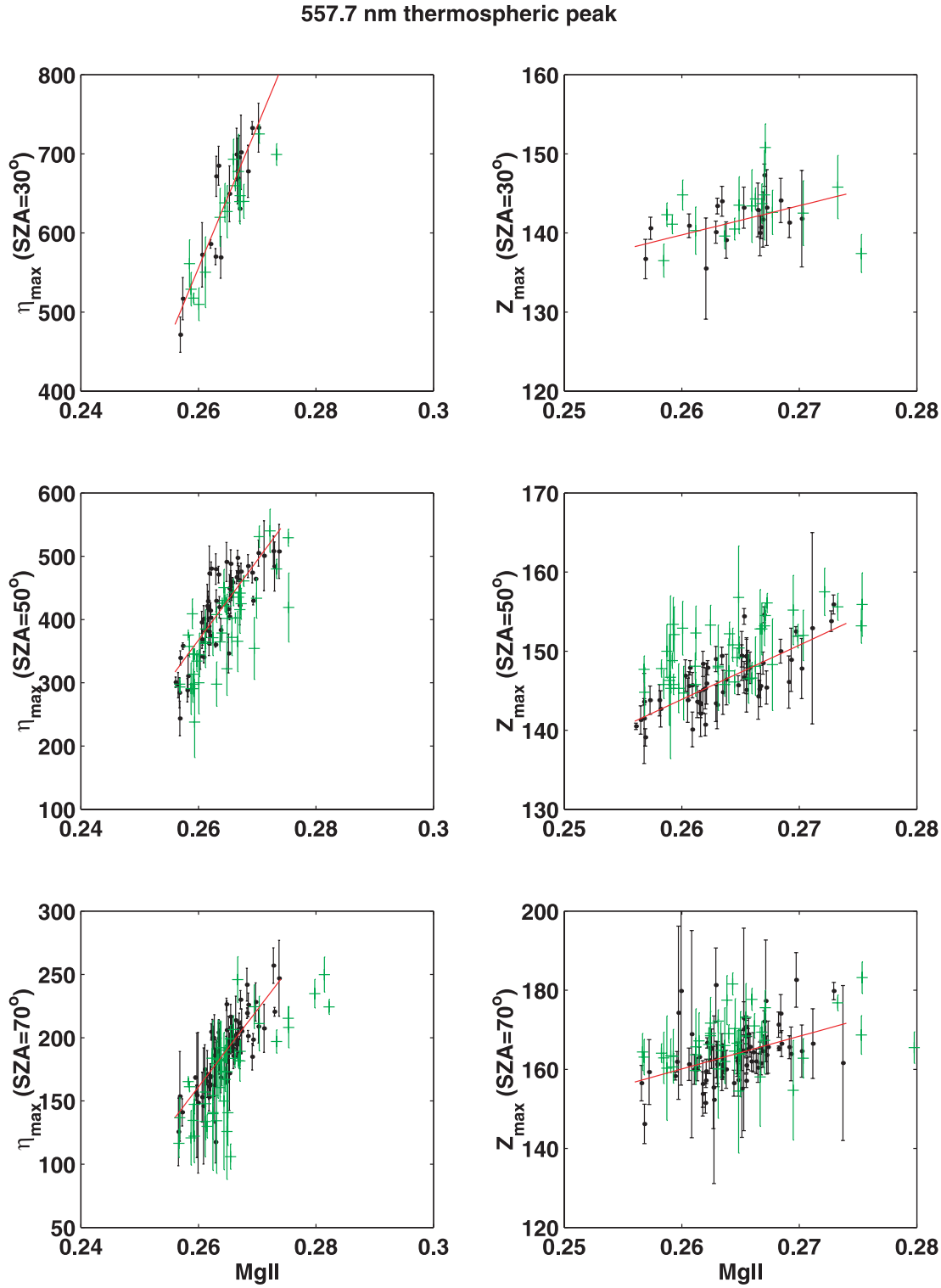

Figure 5. WINDII measurements of the thermospheric peak of the 557.7 nm emission from 1992 to 1995. The volume emission rate (η) is expressed in photons cm^{-3} s^{-1}, and the altitude Z_{max} is expressed in km. Data are plotted versus the Mg II proxy, and error bars correspond to the standard deviation. The black data set corresponds to quiet geomagnetic days ($Ap \leq 10$), the red line being the related linear regression, while the green data set corresponds to stronger geomagnetic activity ($Ap > 30$).